

Visual cohort comparison for spatial single-cell omics-data

Antonios Somarakis, Marieke E. Ijsselsteijn, Sietse J. Luk, Boyd Kenkhuis,
Noel F.C.C. de Miranda, Boudewijn P.F. Lelieveldt, and Thomas Höllt

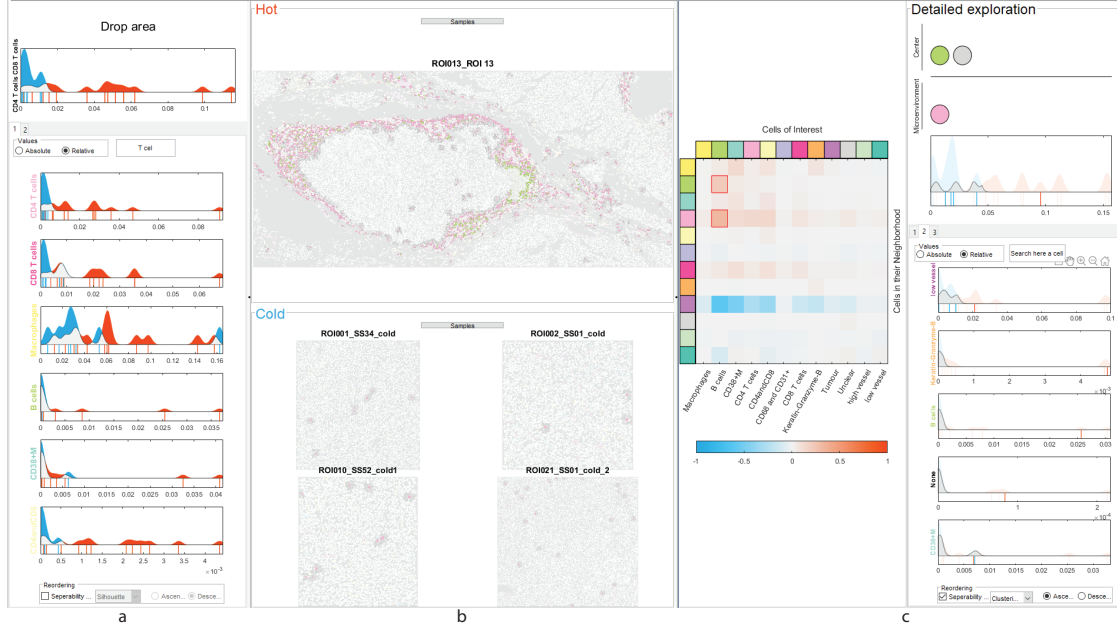


Fig. 1. Screenshot of our integrated system including the view for the comparison based on the cell abundance (a), the tissue view (b), and the multi-cellular microenvironment comparison view (c)

Abstract—Spatially-resolved omics-data enable researchers to precisely distinguish cell types in tissue and explore their spatial interactions, enabling deep understanding of tissue functionality. To understand what causes or deteriorates a disease and identify related biomarkers, clinical researchers regularly perform large-scale cohort studies, requiring the comparison of such data at cellular level. In such studies, with little *a-priori* knowledge of what to expect in the data, explorative data analysis is a necessity. Here, we present an interactive visual analysis workflow for the comparison of cohorts of spatially-resolved omics-data. Our workflow allows the comparative analysis of two cohorts based on multiple levels-of-detail, from simple abundance of contained cell types over complex co-localization patterns to individual comparison of complete tissue images. As a result, the workflow enables the identification of cohort-differentiating features, as well as outlier samples at any stage of the workflow. During the development of the workflow, we continuously consulted with domain experts. To show the effectiveness of the workflow we conducted multiple case studies with domain experts from different application areas and with different data modalities.

Index Terms—Visual analytics, Imaging Mass Cytometry, Vectra, spatially-resolved data, single-cell omics-data, Visual comparison

1 INTRODUCTION

State of the art spatially-resolved omics modalities [10, 14, 16, 20, 24] provide a precise characterization of cellular populations in tissues. Thereby, they enable experts to discover and identify novel cell types [42] among large cohorts of samples. The information about the type of each cell, alongside its specific location creates many heterogeneous multi-cellular patterns. Current research findings [1, 19, 21] underline the clinical importance of analysing such spatial multi-cellular interactions. Hence, such findings make the comparison of spatially-resolved omics-data among cohort of samples with different clinical characteristics crucial for the understanding of tissue functionality.

In the majority of life-science studies, the comparison of cohorts of samples is based on statistical comparison of predefined finite number of elements [29, 30, 34, 45]. However, it is unlikely that a traditional statistical approach can capture the complete space of spatial combinations among all different cell types that can possibly differentiate two cohorts [9]. Comparative visualization [31] can provide useful insights into the differentiating factors of two cohorts.

Here, we present an interactive workflow for the comparison of cohorts consisting of spatial omics-data. The main goal of analysts

- Antonios Somarakis and Boudewijn P.F. Lelieveldt are with the Division of Image Processing, Department of Radiology, Leiden University Medical Center, the Netherlands.
- Marieke E. Ijsselsteijn and Noel F.C.C. de Miranda are with the Immunogenomics group, Department of Pathology, Leiden University Medical Center, the Netherlands.
- Sietse J. Luk is with the Hematology Department, Leiden University Medical Center, the Netherlands.
- Boyd Kenkhuis is with the Human Genetics Departments, Leiden University Medical Center, the Netherlands.
- Thomas Höllt is with the Computer Graphics and Visualization Group, TU Delft and the Leiden Computational Biology Center, Leiden University Medical Center, The Netherlands. E-mail: T.Hollt-1@tudelft.nl

Manuscript received xx xxx. 201x; accepted xx xxx. 201x. Date of Publication xx xxx. 201x; date of current version xx xxx. 201x. For information on obtaining reprints of this article, please send e-mail to: reprints@ieee.org. Digital Object Identifier: xx.xxx/TVCG.201x.xxxxxxx

working with this kind of data is to identify the characteristics that differentiate a cohort, explore the cohorts’ heterogeneity and relate these characteristics directly to the tissue. In some cases, just the comparison of the cell types abundance is adequate to differentiate cohorts. In other cases, a detailed comparison of contained cells and their specific neighborhoods, i.e. microenvironments is needed.

We propose an interactive, data-driven cohort comparison workflow. More specifically the main contributions of this paper are:

1. A spatial omics cohort comparison workflow, addressing the following tasks
 - T1** compare cohorts based on the abundance of different cell types,
 - T2** compare cohorts based on multi-cellular microenvironments,
 - T3** detect outliers within each cohort, and
 - T4** relate findings to their spatial position.
2. The implementation of this workflow

The remainder of this paper is structured as follows. We present related work in section 2, followed by a brief description of the input data and the tasks in section 3. In section 4, we describe our tool and the rationale behind our visual design. The effectiveness of our tool and workflow is shown in the case studies presented in section 5. In section 6 we conclude summarizing lessons learnt from the visual design process and discussing potential directions for future work.

2 RELATED WORK

The visual analytics community spent considerable effort on approaches for the exploration of cohorts of medical data combining spatial and non-spatial features. Preim et al. [32] provide an overview of image-centric approaches [11, 40, 47] focused on the exploration of large imaging cohorts and derived attributes. For the data analysis, these approaches share linking of attribute views with image views to provide context, visual queries for direct feedback, and interactive definition of groups of attributes. They typically deal with traditional medical imaging databases, such as those acquired by computed tomography (CT) or magnet resonance imaging (MRI).

Only recently, spatially-resolved omics-data [10, 14, 20] have become a standard tool for the exploration of tissue structure at the cellular level. Consequently, only few visual analysis tools exist that address the specific needs of this data. Facetto [23] is a scalable framework that allows hierarchical cell type identification in large multiplexed images. histoCAT [36] enables the identification of significant pairwise spatial interactions of different cell types in such data. In our previous work on ImaCytE [39], we employ a fully interactive exploratory pipeline, combining cell type identification and the exploration of multi-cellular spatial interactions patterns. All of the above approaches focus on the analysis of a single data-set or cohort. Here, we introduce the first workflow for comparative analysis of two cohorts of spatially-resolved omics-data.

Based on a survey on existing comparative visualization tools [15], Gleicher et al. define a taxonomy that divides comparative visualization into juxtaposition (side-by-side placement), superposition (layering), and explicit encoding. A large body of work on comparative visualization for individual images exist. For example, Blaas et al. [11] combine superposition with explicit coding of the differences using complementary colors for the comparands, which cancels out in regions without differences. We use the same technique in some of our charts. Lindemann et al. [25], Maries et al. [28] and Ma et al. [27] utilize juxtaposition in an interactive comparative visualization pipeline for one-to-one comparison of segmentation results of brain imaging data. Juxtaposition for the comparison among the images has been also utilized in our work

VAICo [37] by Schmidt et al. facilitates the comparison of image ensembles with small differences. The comparison is performed between all images in the ensemble. The differences of the images are initially

clustered and then presented in an overview first, details on demand fashion. In a similar manner, Raidou et al. [33] compare radiotherapy treatment results of segmented bladders. Zhang et al. [46] introduce a multi-level comparison among two different sets of diffusion tensor images. Basole et al. [4] as well as Wagner et al. [44] propose cohort comparison pipelines, however, limited to non-spatial healthcare data. Their approaches allow for the comparison of the cohorts as a whole, but also among the individual samples of each cohort.

3 ABSTRACTION

Recent developments in the spatially-resolved omics field manifest a wide variety of available modalities [12, 14, 22, 24]. These technologies measure genomics or proteomics information at sub-cellular resolution, resulting in high-resolution image data with tens to thousands of values per pixel. As researchers are interested in this information per cell, rather than per pixel, these images are typically pre-processed by segmenting individual cells and aggregating the values of the segmented pixels. Based on this aggregated information and potentially further features like morphology, the function and type of the segmented cells can be identified [36]. In the following, we abstract the resulting image data cohorts (subsection 3.1) and the analysis tasks (subsection 3.2) when comparing such cohorts.

3.1 Input data

The overarching goal of our workflow is the comparison of two cohorts of spatially-resolved omics data as briefly introduced above. A single cohort consists of a set of samples, i.e., segmented and classified images as described above. Depending on the goal of the study, the samples consist of multiple images from a single subject or an arbitrary number of samples from multiple subjects. Typically, the two cohorts describe different populations, for instance, cancer patients who respond well to treatment in one cohort and those who respond worse in the second. A typical cohort consists of tens to hundreds of images, each consisting of thousands of segmented cells.

In a typical study, tens to hundreds of different cell types will be identified. The granularity depends on the goal of the study, as well as the data modality. For example, our partners using the Vectra System [18], measured the abundance of only 4 different proteins (see subsection 5.3). Assuming differentiation into only low and high abundance, this results in an upper limit of $2^4 = 16$ differentiable cell types. Other systems, such as Imaging Mass Cytometry, allow the measurement of up to 40 proteins, such that the number of cell types is limited rather by what makes biological sense and is of interest for the given study. Here, a broad study would capture in the order of a hundred different cell types.

For each sample, we store the segmentation mask including a cell type, i.e. class, label for each segmented cell. Based on the cell segmentation mask, we derive the microenvironment for each cell. The microenvironment consists of the cell types and their abundance in the neighborhood of the given cell. We store the corresponding information per cell as a list of all cells that are contained in the microenvironment. The microenvironment of a cell varies according to the resolution of the modality and the type of sample. For example, in a tumor crowded with compact cells we would consider cells belonging to the microenvironment in a smaller distance, compared to brain tissue, where interacting cells can be further apart. Therefore, the distance which defines the microenvironment of a cell is specified by the user. Typically, the microenvironment of a cell consists of no more than some tens of cells.

3.2 Identified Tasks

Figure 2 illustrates the main tasks of our workflow and their order in the pipeline. In general, we compare the two cohorts, based on the contained samples. The first step of the workflow is comparing the cohorts according to the abundance of different cell types per sample (**T1**). This allows a simple differentiation of the cohorts based on what cells are contained. In the second step, we further want to find out if the cohorts exhibit differentiating patterns in the cells’ microenvironments.

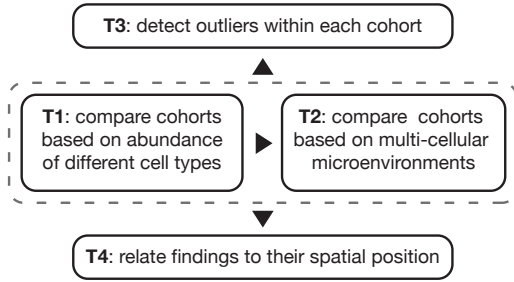


Fig. 2. Overview of the performed tasks in the workflow

Therefore, in **T2** we compare cohorts based on multi-cellular microenvironments. Throughout the process it is also possible to detect outliers within each cohort (**T3**), according to the abundance of contained cells and their microenvironments, and relate any findings to their spatial position (**T4**).

In the following, we describe and abstract **T1-T4** in more detail using Brehmer and Munzners task typology [6]. For references to this typology we use a mono-spaced font.

T1 Cohort comparison based on the abundance of different cell types and combinations thereof in cohort samples. The relative abundance of a cell type in the samples forming a cohort and how much a specific subject deviates from the distribution within the cohort are important clinical biomarkers. As cell types can be of different granularity, it should also be possible to compare the cohorts, based on combinations of cell types. A trivial example is differentiating a cohort of cancer patients and a cohort of healthy subjects by comparing the abundance of cancer cells in the contained samples, where “cancer cells” can be a single cell type, or a combination of cell types according to a more fine grained definition. In this task **T1**, the user compares the two cohorts based on the abundance of different cell types within samples forming the cohort. This enables to discover and locate the cell type(s) that differentiate the two cohorts. The input for **T1** is the abundance of each cell type for each sample that we summarize as distributions over all samples in one cohort. The output is a list of cell types that have been identified as differentiating the two cohorts.

T2 Cohort comparison based on multi-cellular microenvironments. Exploring cell type abundance is only the first step in assessing tissue functionality. Domain researchers hypothesize that cell functionality also depends on the interactions with other cells. The first step to such interactions is that cells are spatially co-located, i.e., the cell’s microenvironment. The goal of task **T2** is to compare the two cohorts according to the co-localization patterns that can be found in each sample. We break this task down into a high-level comparison, based on how often any two cell types are co-located, globally (**T2.a**), and a detail comparison where complex microenvironments can be explored (**T2.b**). In task **T2.a**, the user discovers those combinations of two cell types that are most differentiating between the two cohorts. The input for this task is the abundance of each combination of two cell types in a microenvironment within the cohort sample. The output is a combination of two cell types to be used for further exploration. In task **T2.b**, the user further explores and compares the two cohorts based on more complex microenvironment compositions. Therefore, the user produces these more complex microenvironments by combining different cell types, typically starting with the combination found in **T2.a**. The input for **T2.b** is the complete set of cell microenvironments, optionally filtered to those including the combination of interest discovered in **T2.a**. The output is a set of detailed microenvironments differentiating the two cohorts.

T3 Outlier detection within each cohort. Detecting outliers within a cohort can provide additional important clinical information. For example subjects with different stages of a disease in the same cohort might exhibit different cell profiles [43]. Therefore, **T3** consists of identifying and locating outlying samples and their corresponding features identified in **T1** and **T2**. The input to this task is the abundance of cells and their microenvironments, as identified in **T1** and **T2**. The output is a list of outlying samples.

T4 Relate findings to their spatial position. As described above, **T1-T3** can be carried out based on cell abundance and microenvironment descriptions per sample, without consulting the actual imaging data. However, to verify individual findings we inspect the cells and neighborhoods in their tissue context. Therefore, **T4** relates any findings to their spatial position. The analyst locates the structure of interest in their spatial location and identifies issues that were not apparent in the abstract representation. The input to **T4** are the segmented images and a structure of interest found with **T1-T3**, the output is a verified or rejected finding from **T1-T3**.

4 WORKFLOW

We designed a workflow based on a multiple-linked-views system, shown in Figure 1 to support the four tasks, identified and described in subsection 3.2. Each of the views provides a different view on the data with a specific level of detail to the user. The system is divided in three main blocks. The left block (Figure 1a) supports **T1**, by summarizing the abundance of each cell type over all samples. The middle block (Figure 1b) shows the segmented samples to enable the exploration of structures of interest in their spatial context (**T4**). The right block (Figure 1c) combines multiple views to support the microenvironment exploration (**T2**). All views allow filtering the data to support outlier detection (**T3**). The system is implemented in MATLAB as a stand-alone application. Source code and binaries are available on our GitHub¹ repository.

4.1 Comparison based on cell type abundance

In the first step of the exploration, we are interested in how the two cohorts compare, according to the abundance of the different existing cell types in each of the contained samples (**T1**). Therefore, we first compute the number of cells of each type within each sample and then visualize the distribution of samples within each cohort according to this value. Figure 3a shows these distributions for both cohorts visualized using parameterized raincloud plots [2]. Here, each vertical line represents one sample. The position of each line on x-axis corresponds to the number of cells of a given type within this sample. For easier comparison between differently sized samples, we enable the user to select whether the x-axis should represent number of cells as absolute

¹repository will be made public at the time of publication

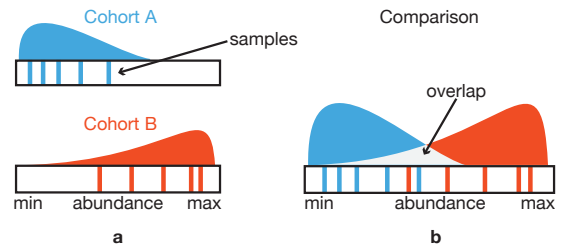


Fig. 3. Comparison of two cohorts for a single feature. (a) The samples in Cohort A (blue lines) generally show a lower abundance of the given feature indicated by their position on the left while the samples in Cohort B (orange lines) show higher abundances. (b) The large difference between the cohorts is immediately visible by the large amount of color and small light-gray overlap area in the area chart.

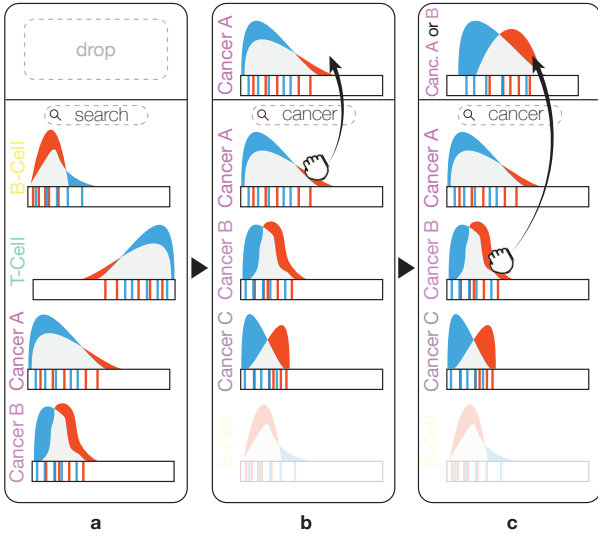


Fig. 4. **Exploration of the raincloud plots set.** Searching for a term in the search field area, reorders the raincloud plots from the default raincloud view (a), placing on top of the list the raincloud plots containing the term in their label (b). Dragging raincloud plots and dropping it in the drop area (b,c), creates progressively every time a new raincloud plot depicting the abundance of the cell types represented from the dropped raincloud plots.

values, or relative to the number of cells in that sample. Additionally, we estimate the probability density function (PDF) of cells per sample using a kernel density estimate and visualize it as an area chart above the lines. Such a visual design offers more information about the distribution of the cohorts (e.g. skewness, outliers) than bar or box-whisker plot and it is more intuitive to read [2].

To facilitate the comparison between the two cohorts we assign a unique color to each cohort and superpose the corresponding raincloud plots (Figure 3b). As our primary goal is the comparison of the two cohorts, rather than the shape of individual plots, we want to emphasize the differences, rather than the commonalities. Therefore, following the same principle as Blaas et. al. [11], we use complementary colors for the two cohorts, i.e. blue and orange and blend the PDFs additively to receive a neutral light-gray in the overlapping areas.

The resulting raincloud plot allows the comparison of the composition of the two cohorts, according to the abundance of a single cell type within the contained samples. To allow the inspection of these distributions for all cell types, we use a small multiples approach [41, Chapter 4] and show the raincloud plots for several cell types in the same view (Figure 1a, Figure 4).

As indicated in subsection 3.1, some studies can contain in the order of 100 different cell types. Finding a specific type of interest or the types that are the most differentiating for the two cohorts manually is not feasible in such a case. We provide two ways to make the exploration of a large set like this more easy. First, we provide filtering, based on the name of cell types by means of a search box above the plots (Figure 4a). To locate a specific cell type of interest, the user can, for example, type *cancer* and all plots corresponding to cell types with the term *cancer* in their provided name will be sorted to appear first in the view (Figure 4b). To explore the cell types that are most interesting with regard to how strongly they differentiate the cohorts we implemented a set of separability metrics (e.g. Silhouette metric [35], Clustering Validation index [17], Dunn’s index [5]) that we use to assign a score to each distribution. The user can sort the plots, according to this score to find those cell types that are the most differentiating.

In some cases, the analyst might also be interested in aggregating the information on several cell types. For example, when several different cancer cell sub-types were identified in the original classification, but the analyst is only interested in how the cancer cells are distributed as

a whole. To that end, we enabled the user to combine cell types, by gradually dragging and dropping the corresponding plots into a drop area on top of the view (Figure 4b,c). The abundances of the dropped cell types are then aggregated as if they were a single cell type and a new distribution is created on-the-fly.

All the views in our system are linked and allow cross-selection. Here, in particular, the user can select each cell type or sample to highlight them in the tissue view (see subsection 4.3) to enable T4. Outlying samples, with regard to a single cell type, can easily be identified in the raincloud plots as lines far from the peaks of the distribution of the same cohort (T3). To further verify whether they are different in more than just one cell type, such samples can be selected by clicking or brushing in the raincloud plot and are then highlighted in the raincloud plots for other cell types.

4.2 Comparison based on cellular microenvironments

The exploration and comparison of the cohorts according to the contained cellular microenvironments is divided into two parts. The first step is to gain a global overview and compare the cohorts based on pairwise co-occurrences of cell types (T2.a). In the second step, the analyst can go into detail, explore and built specific, detailed microenvironments, consisting of an arbitrary number of cell types, and compare the distribution of these microenvironments among the two cohorts (T2.b). Throughout this process, we allow referencing the identified microenvironments with the actual tissue images (T4) and in the second step, samples that are outliers in their cohort, according to the created microenvironment can be identified (T3).

4.2.1 Pairwise Overview

Following ImaCytE [39], we define the microenvironment of a cell as the directly adjacent cells in the tissue. We then compute the frequency for each cell type to occur in each other cell type’s microenvironment throughout the cohort. For a detailed description we refer to our previous work [39, Section 4.3]. The result of this process is a directed and weighted graph, where each node represents a cell type and the link between two nodes defines the frequency of the target node appearing in the microenvironment of the source node. In ImaCytE, we visualize this graph as a heatmap.

Here, we use an explicit coding of the differences between the two cohorts based on the same heatmap layout, illustrated in Figure 5. The vertical axis shows the cell type of interest and the horizontal axis the cell types in the microenvironments. Now, instead of showing the frequencies F , we compute the signed differences D in frequency between the two cohorts C_A and C_B and encode it using color. $D_t(C_A, C_B) = F(C_A) - F(C_B)$. A large positive value indicates that the combination exists predominantly in Cohort A, while a large negative value means the combination predominantly exists in Cohort B. Based on this, we define a simple color map using the same colors previously assigned to the two cohorts and map the maximum absolute value $\max(|D_t|)$ to the color assigned to Cohort A (i.e. blue) and $-\max(|D_t|)$

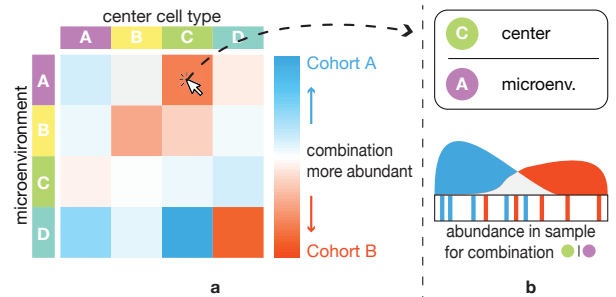


Fig. 5. **Overview of cell type co-localization patterns.** The heatmap (a) explicitly encodes differences in the abundance of pairwise combinations of cell types in the two cohorts. Clicking on one of the combinations sets this combination in the detail view (b), showing the distribution of samples according to the abundance of this combination.

to the color assigned to Cohort B (i.e. orange). Using the same concept of blending between the two colors, described in subsection 4.1, the middle of this colormap, corresponding to $D_t = 0$, will be a neutral light-grey, indicating both cohorts exhibit similar abundance of the given combination (compare Figure 5).

During one of the case studies (subsection 5.1), it became clear that using the relative frequencies, used in ImaCytE [39] and the required normalization biased the heatmap towards differences in small cell populations. To counter this issue, we provide the option to compute the heatmap using the separability metrics, also used for sorting the raincloud plots (subsection 4.1). As these metrics only provide information on how different the cohorts are, we compute the mean abundance of the given cell type combination for all samples in a cohort and use the sign of difference between the two cohorts in combination with the separability metric.

The resulting heatmap effectively shows cell type combinations that differentiate the two cohorts and for which cohort each combination is predominant. The analyst can now further explore individual combinations by clicking the corresponding box in the heatmap. Thereby, the corresponding combination is selected and highlighted in the tissue view (T3) and the microenvironment combination tool for the detail analysis (subsubsection 4.2.2) is pre-populated with the given combination (Figure 6a).

4.2.2 Detail Microenvironments

Starting with the overview of pairwise co-localization patterns, identified with the heatmap visualization, the analyst can now in detail explore complex microenvironment structures, based on any cell type combination and link those to individual samples and their position in the distribution of the corresponding cohort.

In ImaCytE [39], we used a simple glyph to enable the visual exploration of all the existing unique microenvironments in a sample. Here, the focus is on comparing two cohorts with regard to specific microenvironments, that potentially have already been identified as interesting in a previous analysis of the individual cohorts. Therefore, instead of showing all the existing unique microenvironments, we built

an interactive visual query system [38] to quickly combine different cell types to a microenvironment of interest and show how this microenvironment is distributed among the two cohorts. The comparison of the two cohorts then happens with the same raincloud plots introduced in subsection 4.1 but instead of the abundance of a single cell type the plot now shows the abundance of the queried microenvironment.

In practice, the analyst would typically start with a combination of two cell types picked from the heatmap. This simple microenvironment is illustrated on top of the detail view as illustrated in Figure 6a, where it is divided into the cell type of interest in the center of the microenvironment (i.e., cell type A, green circle, Figure 6a) and the microenvironment (i.e., cell type B, purple circle, Figure 6a). For the remainder of the paper we will denote microenvironments as $\bullet | \bullet$, where the circle(s) to the left of the vertical line represents the center cells combined with *or* type and the circle(s) to the right the microenvironment combined with *and*. I.e., a cell from either of the types left of the line must appear in the center and all the types to the right must appear in the surrounding of this cell. Below this (*Selected*, Figure 6a) we show the raincloud plot corresponding to the abundance of all microenvironments with at least the selected combination of cell types. Finally, further below (*Remaining*, Figure 6a) we show the raincloud plots corresponding to the combination of the defined microenvironment plus any of the remaining cell types (here $\bullet | \bullet \emptyset$, $\bullet | \bullet \bullet$, $\bullet | \bullet \bullet$, $\bullet | \bullet \bullet$). The example in Figure 6a starts with *None* (indicated as \emptyset). At first glance it might seem surprising that the corresponding raincloud plot is different from the initial plot above it. *None*, here means that no other additional cell type must exist in the microenvironment, whereas the initial plot shows all microenvironments that at least contain the given types. We denote this as $\bullet | \bullet \emptyset$. Below the *None* plot the remaining combinations are shown with the resulting raincloud plots. As described in subsection 4.1, these plots can be ordered according to how strongly the corresponding microenvironment separates the two cohorts. Figure 6b illustrates the example after reordering. With this information the analyst can now continue exploring the microenvironments, for example by dragging the plot corresponding to cell type B (yellow) to the drop area, creating $\bullet | \bullet \bullet$, (Figure 6b). As the original plot already corresponded to the new microenvironment, we can now simply replace the “Selected” plot with the dragged plot (Figure 6c). The remaining raincloud plots ($\bullet | \bullet \bullet \bullet$, $\bullet | \bullet \bullet \emptyset$, $\bullet | \bullet \bullet \bullet$) are re-computed on-the-fly and shown below. Following this procedure the user can progressively explore all interesting cell type combinations and evaluate their ability to discriminate the two cohorts and as such their potential as biomarkers.

As described in subsection 4.1, the raincloud plots make it easy to identify samples that are outliers in their corresponding cohort (T3). Further, we provide the same linking and brushing features for selecting samples, as described in subsection 4.1, to link the microenvironment patterns to the tissue view (T4).

4.3 Tissue view

In subsection 3.1 we have described the importance of enabling the linking of any finding to its spatial location (T4). Therefore, we provide the tissue view (Figure 7), which shows the original segmented images and, linked to the other views, allows the inspection of selected cell types or microenvironments in the corresponding samples and their spatial context. The tissue view shows the images using color-coding for the different cell types. As we only consider the labeled segmentations as input (subsection 3.1), we use a categorical colormap to assign a color to each label and thus cell type. We have chosen the qualitative *12 class Set 3* from colorbrewer [7] and have excluded blue and orange hues to avoid interference with the cohort colors. This leaves us with only ten different colors, which is typically not enough to assign unique colors to each cell type. Therefore, following the example in ImaCytE [39], we use a semantic cell type hierarchy, where the user can provide or interactively define main cell types and sub-types. We then assign a hue from the color map to each main type if possible and for the sub-types we use different saturation values of the same hue. While not described in detail before, this color scheme is used throughout the application to represent the different cell types and allow for easy mental linking

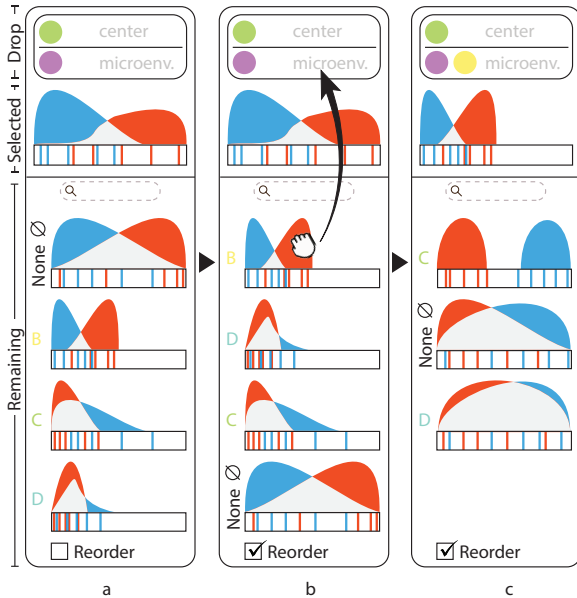


Fig. 6. **Interactive exploration in the detail view.** (a) The abundance of the cells fulfilling the cell type pattern in the “Drop” area is illustrated in the “Selected” raincloud plot. (b) The raincloud plots are reordered in the “Remaining” area, the user drags the first raincloud plot (B) as it separates the cohorts better than the “Selected” one and drop it in the “Drop” area. (c) The dropped raincloud plot replaced the “Selected” one, the “Drop” area and the “Remaining” raincloud plots are updated in order to further assist the exploration.

Table 1. **Summary of the case studies characteristics**, including the imaging modality, the number of samples of each cohort and the number of identified phenotypes in each case study

Case Study ID	Imaging Modality	Number of sample for Cohort 1	Number of sample for Cohort 2	Number of identified phenotypes
Synovial sarcoma	Imaging Mass Cytometry [14]	7	13	12
Tumour metastasis	Imaging Mass Cytometry [14]	19	28	60
Alzheimer disease	Vectra 3.0 (Perkin Elmer) [18]	12	9	16

between views.

To enable comparison between the cohorts, we divide the tissue view into two parts, one for each cohort. As described before, all views are linked. Therefore, the tissue view can be filtered to only show samples selected in other views. Further, selecting cell types or microenvironments in other views highlights them in the images by fading out non-selected structures.

5 VALIDATION

In order to show the effectiveness of our workflow, we conducted three case studies with different collaborators at Leiden University Medical Center. These collaborators all acquired their own data, using two different omics-modalities and have varying analysis goals. For the case studies, we installed our software on the respective participants computers, gave a hands-on introduction and answered any questions regarding the tool. After that, we observed the participants performing their analysis independently and reproduced their workflows for presentation in Sects. 5.1-5.3. As described in section 4, for all the case

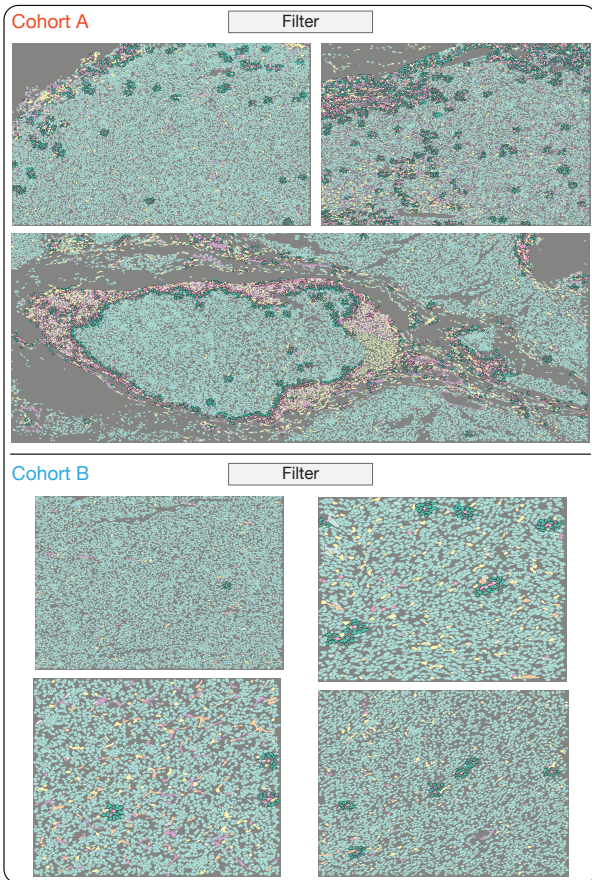


Fig. 7. **Tissue view**, highlighting a spatial interaction fading out the non-selected tissue structures. In the tissue samples of Cohort A, the spatial interactions form a compact structure, whereas the spatial interaction of Cohort B tissue samples are distributed all over the samples.

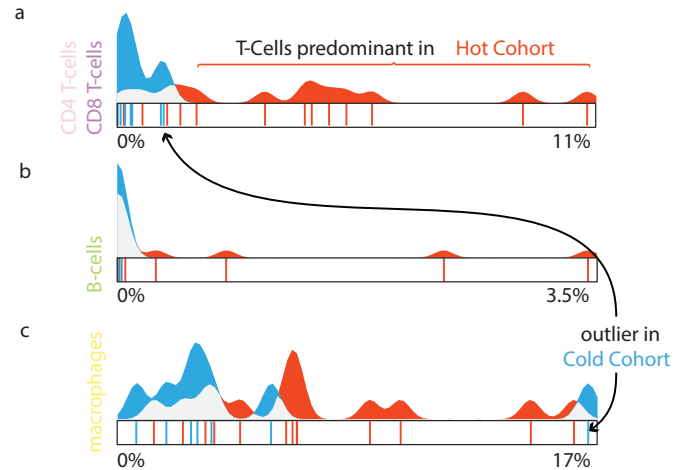


Fig. 8. **Raincloud plots for T-cells (combined, CD4 and CD8) (a), B-cells (b), and macrophages (c).** An outlier for macrophages in Cohort A is clearly visible in (c), selecting it showed it also contained more T-cells than other samples in cohort A (a).

studies the segmentation masks and the cell type identification had been performed as a pre-processing step by the participants. An overview of the study parameters with regard to imaging modality, numbers of samples, and numbers of included cell types is given in Table 1. As can be seen, the studies cover three different application areas, contain data from two different modalities, between 20 and 46 samples, and between 12 and 60 cell types. Finally, we asked the participants, as well as a fourth user of the software who was not part of the case studies, to fill out a short questionnaire (available in the supplemental material) via google forms [13]. The questionnaire consists of the ten standard System Usability Scale (SUS) statements [8], an additional nine statements specific to our tool, answered on a 5-point Likert scale, and five questions for open feedback.

5.1 Case study I: Synovial sarcoma

Synovial sarcoma is a rare form of cancer. During the immune response, T-cells infiltrate the sarcomas. Previous work has shown that synovial sarcomas can have areas with abundant T-cell infiltration (*hot areas*) and areas with very little T-cell infiltration (*cold areas*), in the same tumor [26]. The goal of this case study was to explore differences in the immune cell composition between these two types of areas. A total of 20 areas from 7 different tumors were imaged, of which 7 were cold (*Cold Cohort*, blue) and 13 were hot (*Hot Cohort*, orange). The size of the samples varied, with the number of cells in each image ranging from 2,678 to 23,774 cells. In the pre-processing step, cells were segmented and 12 different cell types were identified, based on the original data. While the number of cell types is relatively low, they cover a large range of available types, with rather coarse specificity.

5.1.1 Cell type abundance

In the first step of the analysis the expert was mostly interested in identifying cell type(s) that differentiate the cohorts, matching **T1** of our task analysis. Given the large variation in the number of cells per sample, he used the relative cell type abundance for comparison.

First, he wanted to explore the uniformity of each cohort. As indicated above, the samples were sorted into the two cohorts based on the infiltration of *T-cells* in the contained tumor tissue. Consequently the *T-cells* should exist predominantly in the Hot Cohort. As a first step the expert wanted to verify this using the system. As there are two different types of *T-cells* in the dataset (*CD4* and *CD8 T-cells*) he first queried for these two cell types and created a combined raincloud plot by dragging the *CD4 T-cell* and *CD8 T-cell* plots to the combined drop area (subsection 4.1). The resulting combined plot (Figure 8a) confirmed that *T-cells* were largely non-existent in all seven samples

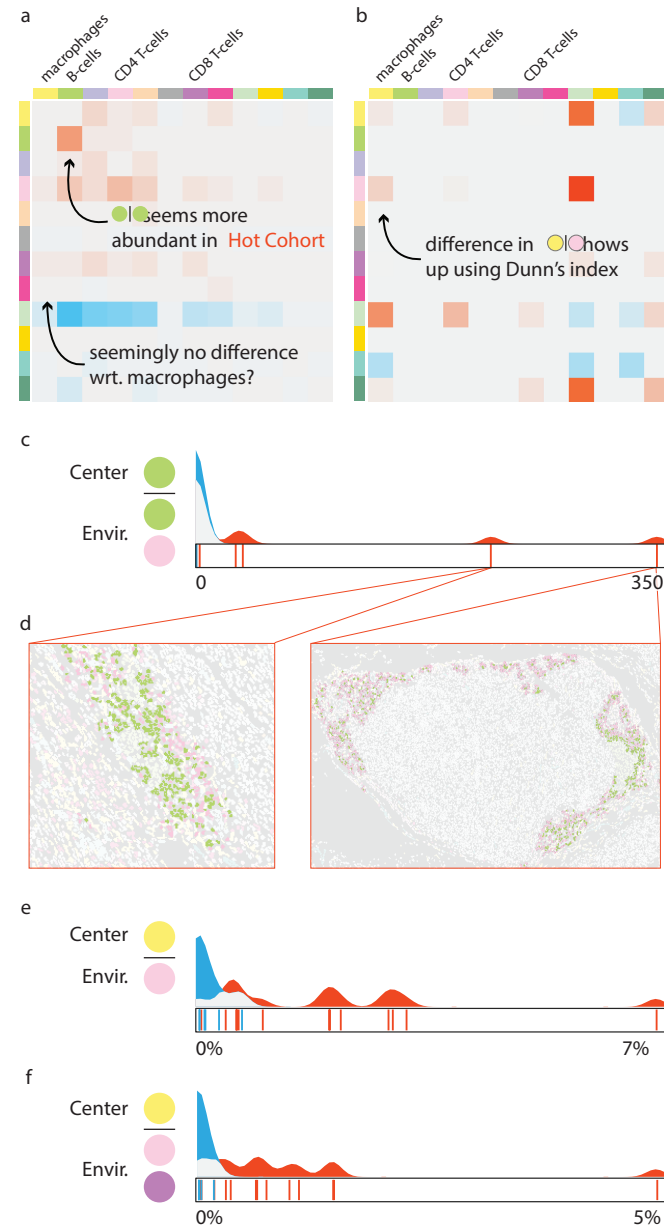


Fig. 9. Multi-cellular microenvironment cohort comparison. (a) A heatmap depicting the difference of the amount of pairwise spatial interaction between two cohorts normalized according to the abundance of each cell type. (b) A heatmap depicting the Dunn index for the samples of each cohort for each pairwise co-localization pattern. (c) The amount of B-cells having in their microenvironment B-cells and CD4 T-cells, depicting that the occurred differentiation in (a) was due to the two outlier samples, which exist in a tertiary lymphoid structure, an interesting biological structure (d). The amount of macrophages having in their microenvironment CD4 T-cells (e) and CD8 T-cells (f).

of the Cold Cohort (blue peak close to 0, Figure 8a) but more widely distributed for the Hot Cohort (even spread of the orange distribution, Figure 8a). Afterwards navigating among the plots, he discovered the raincloud plot for *B-cells* (Figure 8b). This plot caught the experts' interest. Even though most samples from both cohorts hardly contain any B-cells, there are a few samples in the Hot Cohort that contain some B-cells, indicated by the orange lines to the right of the plot in Figure 8b. Given the generally low values, approximately 3 percent, even for the sample with the largest abundance, the expert decided to not further investigate these samples at this point and proceeded with other cell types. Therefore, he ordered the raincloud plots according to the Dunn's index [5]. The first plot illustrating *macrophages* showed a pattern similar to the *T-cells* (Figure 8c). Strikingly, there is an outlier (**T3**) clearly visible in the plot (highlight in Figure 8c). The corresponding sample from the Cold Cohort consists of over 16% macrophages, compared to no more than 5% for all other samples of the same cohort. Selecting the corresponding line in the plot also revealed that this sample has the highest abundance of *T-cells* in this cohort (even though only at around 1% of cells in this sample).

At this point, the expert was curious whether the microenvironments of the macrophages and B-cells could provide further clues on differentiating factors between and within the cohorts.

5.1.2 Microenvironments

The exploration of the differences between the two cohorts, with regard to the contained microenvironments (**T2**) starts with the overview provided by the difference heatmap (Figure 9a). The difference heatmap (Figure 9a) indicated that combinations of B-cells and B-cells (green | green) and B-cells and T-cells (green | pink) were more prevalent in the Hot Cohort (highlighted orange boxes). With this information, the expert created the combined microenvironment (green | green | pink) using the drag and drop interface. The corresponding raincloud plot showed two clear outliers in the Hot Cohort showing a larger abundance of this combination (Figure 9c). Using the linked tissue view, the expert could highlight the microenvironments in the corresponding samples (Figure 9d). The expert observed that the highlighted microenvironments were mostly present in so-called tertiary lymphoid structures [26]. While not directly relevant for the cohort comparison, he noted the two outlier samples for later detailed inspection in his standard workflow.

In the previous step, the expert had also identified macrophages (yellow) for further exploration. Curiously, the heatmap did not show any strong differences between the two cohorts with regard to the microenvironments of this cell type. After the case study we analyzed the data and came to the conclusion that the normalization applied to create the heatmap (subsection 4.2.1) strongly biased the heatmap in favor of small cell populations such as the B-cells in this study (subsection 5.1.1). As a result, we added the option to use the same cluster separation metrics used for sorting the raincloud plots according to their power to separate the cohorts for the heatmap as described in subsection 4.2.1. Figure 9b shows the heatmap using the Dunn's index as an example. Here, the (yellow | pink) microenvironment is more clearly visible, while the small values of the B-Cell microenvironments are suppressed. The expert selected the corresponding box from the heatmap and examined the distribution of the samples for each cohort in the detail view. The blue area around zero (Figure 9e) indicated the absence of (yellow | pink) microenvironment in the Cold Cohort, verifying the heatmap findings. Then, the expert already having identified the correlation among CD8 T-cells and macrophages navigated among the plots of the "Remaining" area of the detail view and located the CD8 T-cell raincloud plot. The addition of CD8 T-cells in the microenvironment of macrophages (yellow | purple) further differentiated the two cohorts, shown by the restriction of the blue area to almost zero (Figure 9f). Even the strong outlier in the Cold Cohort that contained the largest amount of macrophages of all samples did not show any significant co-localization of macrophages and T-cells. On the other hand, several samples in the Hot Cohort showed significant amounts of both combinations. Therefore, the expert concluded that both T-cell sub-types seem to better differentiate the hot and cold tumour areas, than their one-to-one spatial interaction or even their abundances.

5.2 Case study II: Tumour metastasis

In this case study, the expert wanted to explore the differences in the cellular microenvironments of tumours with different clinical characteristics. In particular, she had acquired a data set, consisting of a total of 47 images taken from different tumor samples. Based on other clinical parameters she divided the set in two cohorts. The first one contains 19 images of non-metastatic tumours (*Non-Metastatic Cohort*, orange), the second 28 images of metastatic tumours (*Metastatic Cohort*, blue). She had segmented the images in a pre-processing step and identified 60 different cell types, among a total of 393,727 cells.

5.2.1 Cell type abundance

First, the expert was interested to discover cell type(s) which exist predominantly in one of the cohorts. Given the large amount of cell types, she ordered the raincloud plots according to the Silhouette metric in

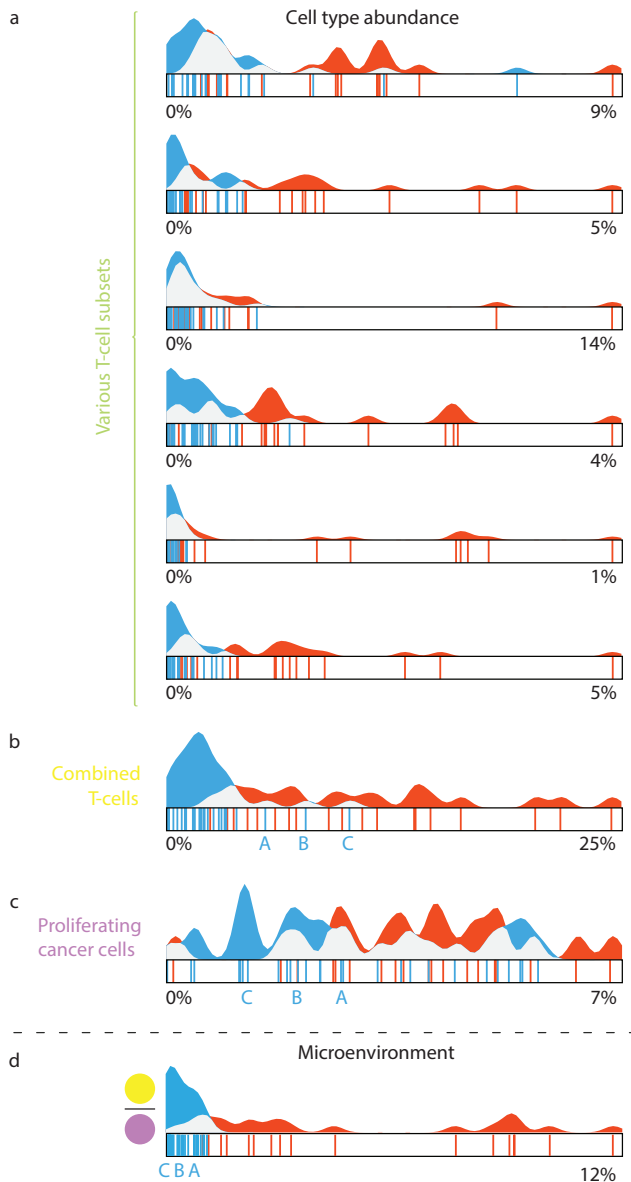


Fig. 10. Raincloud plots for every cell type belonging to the T-cell family (a), the aggregated abundance of T-cells (b), the proliferating cancer cells (c), and the amount of proliferating cancer cells in the microenvironment of T-cells (d). Even though the samples A-C, of the Metastatic Cohort, had a significant amount of T-cells and proliferating cancer cells (b,c) they did not spatially interact (d).

descending order, to assist her exploration. The first few plots consisted mostly of different subsets of T-cells, which had been defined in great detail in the preprocessing step. All of the corresponding plots showed a similar pattern of very small abundances for the Metastatic Cohort, indicated by a large blue peak to the left of the plot and a varying, but generally larger abundance in the Non-Metastatic Cohort. Searching for all cell types containing “T-cell” in their label showed a similar pattern for all of the remaining types (Figure 10a). This pattern is not completely surprising, as T-cells are a major factor in the immune response to cancer. For further exploration, in particular the relation of the identified T-cells to cancer cells, the expert combined all T-cell subsets using the drag and drop interface. The resulting raincloud plot (Figure 10b) confirmed that the T-cells clearly differentiate the two cohorts. There were, however, three samples from the Metastatic Cohort visible (blue lines, labeled A,B,C in Figure 10b) that showed a somewhat increased abundance compared to the remaining samples in that cohort. Next, the expert was interested, whether the increased amount of T-cells in the Non-Metastatic Cohort would correlate to differences in contained tumour cells. The expert searched for “tumour”, to bring up the raincloud plot, corresponding to *Proliferating Tumour Cells*. However, as shown in Figure 10c, no clear separation between the two cohorts can be made, based on these cells. Finally, selecting the three outliers samples (A,B,C) in the T-cell plot did not show a specific differentiation with regard to the tumour cells.

5.2.2 Microenvironments

The last findings of subsection 5.2.1 intrigued the interest of the expert to further explore whether the tumour cells are present in the same amounts also in the microenvironment of T-cells. She quickly combined T-cells and proliferating tumour cells to a microenvironment (Figure 10d) to bring up the corresponding raincloud plot (Figure 10d) in the detail view. The plot shows a clear differentiation among the two cohorts. In fact, this combination differentiates the two cohorts even stronger than only the T-cells. Even for the samples (Samples A,B,C) that showed increased abundance in T-cells, compared to the rest of the Metastatic Cohort, there was only very small abundance of the microenvironment. This strongly indicates that tumour cells exist in the microenvironment of T-cells in the Non-Metastatic Cohort, whereas in the Metastatic Cohort there is no spatial interaction between tumour and T-cells regardless their abundance. This lead the expert to hypothesize that co-localization between the tumour and T-cells need to be taken into account in tumour analysis, rather than abundance of T-cells alone.

5.3 Case study III: Alzheimer’s disease

The accumulation of *amyloid plaques* in the brain is an important characteristic of Alzheimer disease. These amyloid plaques are infiltrated by microglial cells, the resident immune cells of the brain. In this final case study, the expert wanted to verify the hypothesis that the microglia cells close to and potentially attacking amyloid plaques are different from the microglia cells in healthy individuals.

The data used in this case study are somewhat different from the first two cases. The number of samples is comparable. Here, each sample represents one subject, for a total of 12 patients in the Alzheimer’s Cohort (orange) and 9 healthy subjects in the Control Cohort (blue). However, each subject is described by up to 150 images, acquired with the Vectra 3.0 [18] machinery. 16 different cell types were identified and segmented in the pre-processing step. The identified cell types consist mostly of different subsets of microglia cells and as a result, the segmentation of the images is rather sparse, containing only in the order of 25 cells per image, plus the separately segmented amyloid plaques. As such, the individual images were not as important in this study than in the previous two and the data set only contained aggregated information of cell type abundance and microenvironments for all images per subject.

5.3.1 Data analysis

As the experts goal was to verify a specific hypothesis, the data analysis in this study was much more targeted, compared to the rather explorative nature of the previous case studies. First, he brought up the

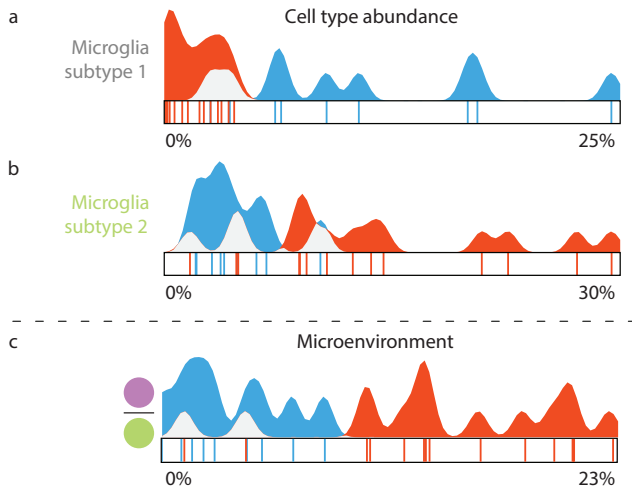


Fig. 11. Raincloud plots for microglia subtype 1(a), subtype 2 (b), and the amount of microglia subtype 2 in the microenvironment of amyloid plaques (d).

raincloud plots corresponding to two microglia subtypes with contradictory patterns (Figure 11a,b). As can be seen in the plots *Subtype 1* (blue) was prevalent in the Control Cohort (blue), whereas *Subtype 2* (orange) was mostly found in samples of the Alzheimer's Cohort (orange) but there was still some overlap between the samples from the two cohorts. This differentiation was already an indicator to verify the original hypothesis of the expert. Going back to the original data, the expert noted that the microglia subtype 2 did not express two proteins that were expressed by Subtype 1 and hypothesized that these proteins might be suppressed when in the vicinity to the amyloid plaques (purple) in Alzheimer's disease patients. Consequently, he brought up the raincloud plot of the corresponding microenvironment (purple) (Figure 11c). Here, the distinction between the two cohorts is even clearer than only for Subtype 2, with only two samples from the Alzheimer's Cohort in the range of the Control Cohort. The distribution further indicates that Subtype 2 seems to co-localize with amyloid plaques, supporting the generated hypothesis.

5.4 Feedback

After the case studies, we collected feedback from the participants using a short questionnaire (available in the supplemental material) via google forms [13]. The questionnaire consists of the ten standard System Usability Scale (SUS) statements [8] (Q1–Q10), an additional nine statements specific to our tool (Q11–Q19), answered on a 5-point Likert scale, and five questions for open feedback. After the case studies, a fourth collaborator started working with the software and we asked her to fill out the same questionnaire after she spent some time with the tool.

The average SUS-score, based on all four questionnaires was 76.25 with a standard deviation of 3.23 resulting in a *good* rating [3]. In the following we briefly summarize the feedback of the custom block of the questionnaire (Q11–Q19), for the complete set of responses we refer to the supplemental material. An overview of the responses is provided in Table 2. The custom part of the questionnaire is divided into three blocks. The first block (Q11–Q14) corresponds to the tasks identified in subsection 3.2. The second block (Q15–Q18) corresponds to the interaction and analysis with the raincloud-based views in the cell abundance and microenvironment exploration. Finally, in the third block, we ask about general feedback.

With statements Q11–Q14 we queried whether **T1–T4** (subsection 3.2) could be carried out efficiently. (Q11; *The tool allows me to efficiently compare two cohorts, according to the abundance of contained cell types per sample.* relates to **T1**, Q12 to **T2**, and so on). Generally, responses were clearly positive with strongly agree (++) or agree (+) with the exception of a neutral (o) response to Q11 and Q12, each. From the open feedback (Q20: *What functionality was*

Table 2. Summary of participants answers to statements of our questionnaire on a 5-point Likert scale from very positive (++) to negative (-). No very negative (-) responses were given.

Q	11	12	13	14	15	16	17	18	19
++	••		••	•	••	•	•		
+	•	•••	••	•••	••	••	•••	•	••
o	•	•				•		•••	
-									••

missing to fully accomplish all goals?) we could gather that participants would like to be able to “correct[ion] cell abundance” with regard to the amount of cells from user-defined area. Further, “statistical testing of differences found between cohorts” was requested, related to **T1** and **T2**.

In Q15–Q18 we were interested whether the raincloud plots were helpful to compare the distributions (Q15, **T1–T2**) and to find outliers (Q16, **T3**) as well as whether the drag and drop interaction made it easy to combine cell types (Q17) and build microenvironments (Q18). Q15–Q17 were overwhelmingly positive, with Q18 getting neutral responses by majority. The different response to Q17 and Q18 is not entirely clear to us, as the interaction for combining cell types and building the detailed microenvironments is essentially the same. Unfortunately, there is also no further feedback on this in the open part of the questionnaire.

In Q19 we wanted to know whether the participants *could accomplish all my [their] exploration/analysis goals*. The responses were split between agree and disagree. In the open feedback we can see that Participant 3 was missing “*Within subject distribution of celltypes/clusters.*” As described in Figure 5.3, we had aggregated the very large amount of images in this study to a single dataset per subject. It might be interesting to provide a hierarchical approach in the future, that allows drilling into these subjects. Participant 4 mentioned “*the option to compare 3 cohorts*” as a missing feature in the open feedback. While the focus of this work is on comparison between two cohorts this constitutes certainly an avenue for future work.

Finally, in the open feedback the “*possibility to detect outliers (and directly identify the subject)*” (**T3**) was specifically mentioned as a positive aspect. The link between the abstract views and the actual images (**T4**) was highlighted by one participant: “*The rainbowplots are really cool, especially because you can go up and down to the images again.*” Particularly positive was a comment by Participant 1, that “*with the tool I already discovered a very nice thing in my existing data!*”.

6 CONCLUSION AND FUTURE WORK

We presented a workflow for the interactive visual comparison of two cohorts comprising single-cell omics-data, based on the cell abundance and cell microenvironments. During the workflow, we enable the user to detect possible outliers in each cohort and locate the spatial location of the findings. We implemented the workflow in a multiple-linked-views system. The main component of our system offers simultaneously cohort comparison and outlier detection, is a modified raincloud plot showing two distributions. Moreover, in order to enable the comparison of cohorts based on all possible cellular microenvironments, we built a visual query system. We illustrated the effectiveness of our workflow through three different case studies using two different modalities and with varying input characteristics. In all of the case studies, the expert users were able to discover biologically relevant tissue structures or characteristics capable of differentiating the clinical cohorts.

The comparison of two cohorts does not cover the entirety of clinical comparison studies. Comparison between more than two clinical cohorts or of the same cohort at multiple time-points is a possible extension of our project. It would also be interesting to combine the system with more detailed in-cohort data exploration tools such as our previous work on ImaCytE, for example, to allow the experts to immediately follow up with detailed analysis of outliers found within a cohort.

REFERENCES

- [1] H. R. Ali, H. W. Jackson, V. R. T. Zanotelli, E. Danenberg, J. R. Fischer, H. Bardwell, E. Provenzano, O. M. Rueda, S.-F. Chin, S. Aparicio, C. Caldas, and B. Bodenmiller. Imaging mass cytometry and multiplatform genomics define the phenogenomic landscape of breast cancer. *Nature Cancer*, 1(2):163–175, 2020. doi: 10.1038/s43018-020-0026-6
- [2] M. Allen, D. Poggiali, K. Whitaker, T. R. Marshall, and R. Kievit. Raincloudplots tutorials and codebase (version v1.0), 2018. doi: 10.7287/peerj.preprints.27137v1
- [3] A. Bangor, P. Kortum, and J. Miller. Determining what individual SUS scores mean: Adding an adjective rating scale. *Journal of Usability Studies*, 3:114–1234, 1996.
- [4] R. C. Basole, H. Park, M. Gupta, M. L. Braunstein, D. H. Chau, M. Thompson, V. Kumar, R. Pienta, and M. Kahng. A visual analytics approach to understanding care process variation and conformance. In *Proceedings of the Workshop on Visual Analytics in Healthcare (VAHC)*, 2015. doi: 10.1145/2836034.2836040
- [5] J. C. Bezdek and N. R. Pal. Cluster validation with generalized dunn’s indices. In *Proceedings of Artificial Neural Networks and Expert Systems (ANNES)*, pp. 190–193, 1995. doi: 10.1109/ANNES.1995.499469
- [6] M. Brehmer and T. Munzner. A multi-level typology of abstract visualization tasks. *IEEE Transactions on Visualization and Computer Graphics*, 19(12):2376–2385, 2013. doi: 10.1109/TVCG.2013.124
- [7] C. A. Brewer, G. W. Hatchard, and M. A. Harrower. ColorBrewer in print: A catalog of color schemes for maps. *Cartography and Geographic Information Science*, 30(1):5–32, 2003. doi: 10.1559/152304003100010929
- [8] J. Brooke. SUS: a “quick and dirty” usability scale. In P. W. Jordan, B. Thomas, B. A. Weerdmeester, and I. L. McClelland, eds., *Usability Evaluation in Industry*, pp. 189–194. Taylor and Francis, 1996.
- [9] L. Cibulski and B. Preim. Visual analytics support for analysis of cohort study data: Requirements and concepts. Technical report, Otto-Von-Guericke University Magdeburg, 2016.
- [10] N. Crosetto, M. Bienko, and A. Van Oudenaarden. Spatially resolved transcriptomics and beyond. *Nature Reviews Genetics*, 16(1):57–66, 2015. doi: 10.1038/nrg3832
- [11] O. Dzyubachyk, J. Blaas, C. P. Botha, M. Staring, M. Reijnierse, J. L. Bloem, R. J. Van Der Geest, and B. P. Lelieveldt. Comparative exploration of whole-body MR through locally rigid transforms. *International Journal of Computer Assisted Radiology and Surgery*, 8(4):635–647, 2013. doi: 10.1007/s11548-013-0820-z
- [12] A. M. Femino, F. S. Fay, K. Fogarty, and R. H. Singer. Visualization of single rna transcripts in situ. *Science*, 280(5363):585–590, 1998. doi: 10.1126/science.280.5363.585
- [13] Google forms. <https://www.google.com/forms/about/>. Accessed: 2020-04-20.
- [14] C. Giesen, H. A. Wang, D. Schapiro, N. Zivanovic, A. Jacobs, B. Hattendorf, P. J. Schöffler, D. Grolimund, J. M. Buhmann, S. Brandt, Z. Varga, P. J. Wild, D. Günther, and B. Bodenmiller. Highly multiplexed imaging of tumor tissues with subcellular resolution by mass cytometry. *Nature Methods*, 11(4):417–422, 2014. doi: 10.1038/nmeth.2869
- [15] M. Gleicher, D. Albers, R. Walker, I. Jusufi, C. D. Hansen, and J. C. Roberts. Visual comparison for information visualization. *Information Visualization*, 10(4), 2011. doi: 10.1177/1473871611416549
- [16] Y. Goltsev, N. Samusik, J. Kennedy-Darling, S. Bhate, M. Hale, G. Vazquez, S. Black, and G. P. Nolan. Deep profiling of mouse splenic architecture with codex multiplexed imaging. *Cell*, 174(4):968–981.e15, 2018. doi: 10.1016/j.cell.2018.07.010
- [17] M. Halkidi and M. Vazirgiannis. Clustering validity assessment: Finding the optimal partitioning of a data set. In *Proceedings of IEEE International Conference on Data Mining (ICDM)*, pp. 187–194, 2001. doi: 10.1109/icdm.2001.989517
- [18] M. E. Ijsselstein, T. P. Brouwer, Z. Abdulrahman, E. Reidy, A. Ramalheiro, A. M. Heeren, A. Vahrmeijer, E. S. Jordanova, and N. F. de Miranda. Cancer immunophenotyping by seven-colour multispectral imaging without tyramide signal amplification. *The Journal of Pathology: Clinical Research*, 5:3–11, 2019. doi: 10.1002/cjp2.113
- [19] H. W. Jackson, J. R. Fischer, V. R. Zanotelli, H. R. Ali, R. Mechera, S. D. Soysal, H. Moch, S. Muenst, Z. Varga, W. P. Weber, and B. Bodenmiller. The single-cell pathology landscape of breast cancer. *Nature*, 578(7796):615–620, 2020. doi: 10.1038/s41586-019-1876-x
- [20] R. Ke, M. Mignardi, A. Pacureanu, J. Svedlund, J. Botling, C. Wählby, and M. Nilsson. In situ sequencing for rna analysis in preserved tissue and cells. *Nature Methods*, 10(9):857–860, 2013. doi: 10.1038/nmeth.2563
- [21] L. Keren and M. Angelo. Mapping cell phenotypes in breast cancer. *Nature Cancer*, 1(2):156–157, 2020. doi: 10.1038/s43018-020-0031-9
- [22] L. Keren, M. Bosse, S. Thompson, T. Risom, K. Vijayaragavan, E. McCaffrey, D. Marquez, R. Angoshtari, N. F. Greenwald, H. Fienberg, J. Wang, N. Kambham, D. Kirkwood, G. Nolan, T. J. Montine, S. J. Galli, R. West, S. C. Bendall, and M. Angelo. MIBI-TOF: a multiplexed imaging platform relates cellular phenotypes and tissue structure. *Science Advances*, 5(10):eaax5851, 2019. doi: 10.1126/sciadv.aax5851
- [23] R. Krueger, J. Beyer, W. D. Jang, N. W. Kim, A. Sokolov, P. K. Sorger, and H. Pfister. Facetto: Combining unsupervised and supervised learning for hierarchical phenotype analysis in multi-channel image data. *IEEE Transactions on Visualization and Computer Graphics*, 26(1):227–237, 2020. doi: 10.1109/TVCG.2019.2934547
- [24] J. H. Lee, E. R. Daugherty, J. Scheiman, R. Kalhor, T. C. Ferrante, R. Terry, B. M. Turczyk, J. L. Yang, H. S. Lee, J. Aach, K. Zhang, and G. M. Church. Fluorescent in situ sequencing (FISSEQ) of rna for gene expression profiling in intact cells and tissues. *Nature Protocols*, 10(3):442–458, 2015. doi: 10.1038/nprot.2014.191
- [25] F. Lindemann, K. Laukamp, A. H. Jacobs, and K. Hinrichs. Interactive comparative visualization of multimodal brain tumor segmentation data. In *Proceedings of Vision, Modeling & Visualization (VMV)*, 2013. doi: 10.2312/PE.VMV.VMV13.105-112
- [26] S. J. Luk, D. M. der Steen, R. S. Hagedoorn, E. S. Jordanova, M. W. Schilham, J. V. Bovée, A. H. Cleven, J. F. Falkenburg, K. Szuhai, and M. H. Heemskerk. PRAME and HLA Class I expression patterns make synovial sarcoma a suitable target for PRAME specific t-cell receptor gene therapy. *Oncotarget*, 7(12):e1507600, 2018. doi: 10.1080/2162402X.2018.1507600
- [27] C. Ma, F. Pellolio, D. A. Llano, K. A. Stebbings, R. V. Kenyon, and G. E. Marai. RemBrain: exploring dynamic biospatial networks with mosaic matrices and mirror glyphs. *Journal of Imaging Science and Technology*, 61(6):0–1, 2017. doi: 10.2352/J.ImagingSci.Technol.2017.61.6.000000
- [28] A. Maries, N. Mays, M. Hunt, K. F. Wong, W. Layton, R. Boudreau, C. Rosano, and G. E. Marai. GRACE: a visual comparison framework for integrated spatial and non-spatial geriatric data. *IEEE Transactions on Visualization and Computer Graphics*, 19(12):2916–2925, 2013. doi: 10.1109/TVCG.2013.161
- [29] A. Nagaishi, M. Takagi, A. Umemura, M. Tanaka, Y. Kitagawa, M. Matsui, M. Nishizawa, K. Sakimura, and K. Tanaka. Clinical features of neuromyelitis optica in a large japanese cohort: Comparison between phenotypes. *Journal of Neurology, Neurosurgery and Psychiatry*, 82(12):1360–1364, 2011. doi: 10.1136/jnnp-2011-300403
- [30] C. J. Newschaffer, K. Otani, M. K. McDonald, and L. T. Penberthy. Causes of death in elderly prostate cancer patients and in a comparison nonprostate cancer cohort. *Journal of the National Cancer Institute*, 92(8):613–621, 2000. doi: 10.1093/jnci/92.8.613
- [31] H.-G. Pagendarm and F. H. Post. Comparative visualization: Approaches and examples. In M. Gbel, H. Miller, and B. Urban, eds., *Visualization in Scientific Computing*. Springer, 1995.
- [32] B. Preim, P. Klemm, H. Hauser, K. Hegenscheid, S. Oeltze, K. Toennies, and H. Völzke. Visual analytics of image-centric cohort studies in epidemiology. In L. Linsen, B. Hamann, and H. C. Hege, eds., *Visualization in Medicine and Life Sciences III. Mathematics and Visualization*, pp. 221–248. Springer, 2016. doi: 10.1007/978-3-319-24523-2_10
- [33] R. Raidou, O. Casares-Magaz, A. Amirkhanov, V. Moiseenko, L. Muren, J. Einck, A. Vilanova, and M. Gröller. Bladder Runner: Visual analytics for the exploration of rt-induced bladder toxicity in a cohort study. *Computer Graphics Forum*, 37(3):205–216, 2018. doi: 10.1111/cgf.13413
- [34] C. Robert, A. Ribas, J. D. Wolchok, F. S. Hodi, O. Hamid, R. Kefford, Weber, J. S. A. M. Joshua, W.-J. Hwu, T. C. Gangadhar, A. Patnaik, R. Dronca, H. Zarour, R. W. Joseph, P. Boasberg, B. Chmielowski, C. Mateus, M. A. Postow, K. Gergich, J. Ellassaia-Schaap, X. N. Li, R. Iannone, S. W. Ebbinghaus, S. P. Kang, and A. Daud. Anti-programmed-death-receptor-1 treatment with pembrolizumab in ipilimumab-refractory advanced melanoma: A randomised dose-comparison cohort of a phase 1 trial. *The Lancet*, 384(9948):1109–1117, 2014. doi: 10.1016/S0140-6736(14)60958-2
- [35] P. J. Rousseeuw. Silhouettes: A graphical aid to the interpretation and validation of cluster analysis. *Journal of Computational and Applied Mathematics*, 20(C):53–65, 1987. doi: 10.1016/0377-0427(87)90125-7
- [36] D. Schapiro, H. W. Jackson, S. Raghuraman, J. R. Fischer, V. R. Zanotelli, D. Schulz, C. Giesen, R. Catena, Z. Varga, and B. Bodenmiller. HistoCAT:

analysis of cell phenotypes and interactions in multiplex image cytometry data. *Nature Methods*, 14(9):873–876, 2017. doi: 10.1038/nmeth.4391

- [37] J. Schmidt, M. E. Gröller, and S. Bruckner. VAICo: visual analysis for image comparison. *IEEE Transactions on Visualization and Computer Graphics*, 19(12):2090–2099, 2013. doi: 10.1109/TVCG.2013.213
- [38] B. Shneiderman. Dynamic queries for visual information seeking. *IEEE Software*, 11(6):70–77, 1994. doi: 10.1109/52.329404
- [39] A. Somarakis, V. Van Unen, F. Koning, B. P. Lelieveldt, and T. Höllt. ImaCytE: visual exploration of cellular microenvironments for imaging mass cytometry data. *IEEE Transactions on Visualization and Computer Graphics*, pp. 1–1, 2019. doi: 10.1109/tvcg.2019.2931299
- [40] M. D. Steenwijk, J. Milles, M. Buchem, J. Reiber, and C. P. Botha. Integrated visual analysis for heterogeneous datasets in cohort studies. In *Proceedings of the Workshop on Visual Analytics in Healthcare (VAHC)*, 2010.
- [41] E. R. Tufte. *Envisioning information*. Graphics Press, 1990.
- [42] V. Van Unen, T. Höllt, N. Pezzotti, N. Li, M. J. Reinders, E. Eisemann, F. Koning, A. Vilanova, and B. P. Lelieveldt. Visual analysis of mass cytometry data by hierarchical stochastic neighbour embedding reveals rare cell types. *Nature Communications*, 8(1):1–10, 2017. doi: 10.1038/s41467-017-01689-9
- [43] V. van Unen, N. Li, I. Molendijk, M. Temurhan, T. Höllt, A. E. van der Meulen-de Jong, H. W. Verspaget, M. L. Mearin, C. J. Mulder, J. van Bergen, B. P. Lelieveldt, and F. Koning. Mass cytometry of the human mucosal immune system identifies tissue- and disease-associated immune subsets. *Immunity*, 44(5):1227–1239, 2016. doi: 10.1016/j.immuni.2016.04.014
- [44] M. Wagner, D. Slijepcevic, B. Horsak, A. Rind, M. Zeppelzauer, and W. Aigner. KAVAGait: knowledge-assisted visual analytics for clinical gait analysis. *IEEE Transactions on Visualization and Computer Graphics*, 25(3):1528–1542, 2019. doi: 10.1109/TVCG.2017.2785271
- [45] Y. Yuan, H. Failmezger, O. M. Rueda, H. Raza Ali, S. Gräf, S. F. Chin, R. F. Schwarz, C. Curtis, M. J. Dunning, H. Bardwell, N. Johnson, S. Doyle, G. Turashvili, E. Provenzano, S. Aparicio, C. Caldas, and F. Markowitz. Quantitative image analysis of cellular heterogeneity in breast tumors complements genomic profiling. *Science Translational Medicine*, 4(157):157ra143–157ra143, 2012. doi: 10.1126/scitranslmed.3004330
- [46] C. Zhang, T. Höllt, M. W. A. Caan, E. Eisemann, and A. Vilanova. Comparative visualization for diffusion tensor imaging group study at multiple levels of detail. In *Proceedings of Visual Computing for Biology and Medicine (VCBM)*, pp. 53–62, 2017. doi: 10.2312/vcbm.20171237
- [47] Z. Zhang, D. Gotz, and A. Perer. Interactive visual patient cohort analysis. In *Proceedings of the Workshop on Visual Analytics in Healthcare (VAHC)*, 2012.